Parameter design of a biaxial lidar ceilometer

Eduard Gregorio,[1] Francesc Rocadenbosch,[2] Jordi Tiana-Alsina,[2]
Adolfo Comerón,[2] Ricardo Sanz,[3] and Joan R. Rosell[3]

[1]*Department of Agroforestry Engineering,*
Universitat de Lleida, Campus de Cappont, Edifici CREA,
C/ Pere de Cabrera s/n, 25001 Lleida, Spain
email: egregorio@eagrof.udl.cat

[2]*RSLab, Department of Signal Theory and Communications,*
Universitat Politècnica de Catalunya, Campus Nord,
Edifici D4, C/ Jordi Girona 1-3, 08034 Barcelona, Spain

[3]*Department of Agroforestry Engineering,*
Universitat de Lleida, Campus ETSEA, Edifici 4,
Avda. Rovira Roure 191, 25198 Lleida, Spain

This paper presents parameter design methodology and related opto-mechanical engineering of a 905-nm diode-laser biaxial, eye-safe lidar ceilometer prototype for cloud-height monitoring. Starting with a brief review of the state-of the-art ceilometer technology, acceptable parameter ranges are identified for the key system parts. Parameter tuning is achieved by imposing goal criteria on the simulated signal-to-noise ratio (SNR) and laser-telescope overlap factor. The system is based on a low-cost pulsed semiconductor laser, low-cost Fresnel-lens telescope, a low-NEP avalanche-photodiode opto-electronic receiver, and collimating/focusing adjustable parts. Finally, preliminary test measurements are presented.

Keywords: lidar, opto-mechanical design, signal-to-noise ratio, clouds.

I. INTRODUCTION

Lidar technology based on ceilometers enable high resolution (distance and time) determination of cloud base heights and are commonly used in airports to ensure air traffic safety [1], as well as in weather and scientific stations. Several commercial models are presently available in the market. Their operating principle normally entails the emission of laser pulses at high repetition-frequency rates and with low energy content, obtaining the signal-to-noise ratios required for data inversion and/or real-time data processing through pulse averaging [2]. This configuration has enabled the development of small-sized and eye-safe lidar ceilometers, which cost less than conventional lidar systems. Despite these achievements, major shortcomings are presented in the scientific literature concerning the methodologies applied to the design of these instruments. Most work is based on the final specifications of the ceilometers, while the finer details of the opto-mechanical solutions that have been implemented are commonly not discussed as they may well involve commercial/industrial interests and/or patented results.

The prototype developed by the authors is conceived as an affordable and eye-safe instrument, capable of determining rain-cloud heights, and operates as a cooperative sensor for storm forecasting. A maximum range of 7.5 km is considered sufficient for these purposes. Similar detection ranges can be found in commercial ceilometers [3]-[9]. A biaxial configuration is chosen because of its greater simplicity and since the aim is not the detection of surface fogs.

The paper is largely design and methodologically oriented with special emphasis on the design and prototype engineering of both the optical and mechanical aspects concerning the ceilometer emission and receiving subsystems. Step-by-step applied-design methodology is presented. Section II presents the most relevant design parameters of a lidar ceilometer. Section III presents the simulations carried out to assess the prototype design parameters. Section IV is devoted to the main core of the prototype design and covers both the emission and receiving subsystems. In Sect. V, the constructed prototype and the first-test measurements are presented. Finally, Sect. VI gives concluding remarks.

II. STATE-OF-THE-ART: DESIGN PARAMETERS

In what follows we present the main variables that must be taken into account in order to design a lidar ceilometer with the desired performance. To that aim we divide the section into three parts. In the first two parts, the design parameters of the emission and receiver subsystems are respectively discussed. In the third, two possible ceilometer configurations are discussed.

A. Emission subsystem

Commercial lidar ceilometers usually use pulsed laser diodes, with wavelengths of around 900 nm and repetition frequencies of a few kHz, as light sources. Main advantages are the low cost of laser diodes, their ease of operation, and the extensive availability of photodetectors at these wavelengths. The duration of the laser pulses, is usually between τ_L =10 and 150 ns [2, 10], and the sampling frequencies (f_s), between 20 and 100 $MSps$ (10^6 samples per second) with equivalent detection time $\tau_d = \frac{1}{f_s}$, all of which enables spatial resolutions ($\Delta R = \frac{c(\tau_L+\tau_d)}{2}$ [11]), between 3 and 30 m [12, 13].

As mentioned above, while the low-cost laser diodes are the predominant solution in commercial systems, it should also be noted the development of some instruments based on solid-state lasers, including the Jenoptik CHM15k model [7], whose transmission source is a 1064 nm Nd:YAG laser.

Emission wavelength, λ

As for eye-safe wavelengths ($\sim$1.5 μm in Ref. [14]), some experimental prototypes have been designed [15] and even some commercial models [16] based on Erbium-doped glass laser. While at 1.5 μm it is possible to significantly increase the energy emitted and meet eye safety requirements, its application is limited because of the scant availability of photodetectors, generally InGaAs-APD with very small diameters ($d_D \leq 200\ \mu m$) and low detectivities [17]. For these reasons the preferred option is a 905 nm design.

Energy pulse characteristics

Since commercial lidar ceilometers normally use laser diodes of high pulse repetition fre-

quency (PRF) with energies in the interval between 1 and 10 μJ [2, 18], eye safety at 900-nm wavelength is ensured by expanding the laser beam with a consequent reduction of radiant exposure (Jm^{-2}). The expansion optics also enables minimization of laser beam divergence, which in laser diodes has an elliptical shape and values of the order of $10^o \times 30^o$, to a few milliradians.

B. Receiving subsystem

A classical ceilometer receiving subsystem consists of three main elements:

- Optics to capture and focus the backscattered lidar signal, where the primary lens (system aperture) usually has a diameter (d_0), ranging between 100 and 200 mm [2, 5].

- Interference filter (in the nm range) to select the radiation at the wavelength of interest.

- Photodetector module responsible for transducing the light into an electrical signal. At 900 nm this usually consists of the combination of a silicon avalanche photodiode ($Si\text{-}APD$) and a transimpedance amplifier (TIA). Using $Si\text{-}APDs$, intrinsic responsivities (R_{io}) between 0.30 and 0.62 A/W can be obtained, at a much lower cost than photomultiplier tubes (PMT), corresponding to quantum efficiencies (QE) between 40 and 85 % [19], with gains (M) commonly ranging between 30 and 250. The Noise Equivalent Power of the module (NEP_m) is proportional to the square root of the photosensitive detector area (diameters between 0.25 and 5 mm) and to the bandwidth B_N of the photodetector module [17]. The NEP_m, commonly takes values from 20 to 700 $fWHz^{-1/2}$ in Ref. [20].

- Diaphragm aperture working as a spatial filter, to achieve both a large field of view and a high background-rejection ratio [21, 22].

Field of View, FOV

The field of view must be greater than the laser beam divergence so that the atmospheric cross-section illuminated by the laser is fully seen within the receiver FOV. The FOV in commercial ceilometers is usually between 0.5 and 5 $mrad$ (half-angle). For final specification of this parameter account should be taken of the fact that narrow fields of view reduce

background radiation and the effects of multiple scattering, while for higher values full overlap is achieved at low elevations and alignment between the emission and reception axes of the system is facilitated.

C. Ceilometer configuration

When conceptualizing a lidar ceilometer, one of the key parameters for assessment of its detection capacity is the measurement range or distance interval in which the clouds can be detected. Two ceilometer "families" can be distinguished in terms of their maximum range:

- Systems, such as the All Weather, Inc. model 8339 [3], the Eliasson Engineering CBME80 model [4] or the Vaisala CL31 ceilometer [5], which measure up to an approximate altitude of 7.5 km. (The citation of instruments or manufacturers does not constitute an endorsement or preferential treatment by the authors or by the project funding entities).

- Specially designed systems for high-altitude cirrus detection with a maximum range between 12 and 15 km. Such systems include the All Weather, Inc. model 8340 [6], the Jenoptik CHM15k model [7] or the Vaisala CL51 [8].

The minimum sounding range of the instrument depends fundamentally on whether it has a coaxial or biaxial configuration. Coaxial ceilometers have a single emission-reception axis with the laser beam always within the FOV of the telescope. This enables detection from elevations of virtually zero and is extremely useful for monitoring low altitude phenomena. However, a coaxial configuration has the drawback of internal optical cross talk, which means electronic compensation systems have to be incorporated as in Vaisala's CT25k model [9], or the development of ad-hoc optical solutions as in the Vaisala CL31 [5], which incorporates a special lens with an outer area responsible for focussing backscattered light onto the photoreceptor and a central area responsible for laser beam collimation. In contrast, one of the characteristic features of biaxial ceilometers is their different emission and reception optical axes. Biaxial configuration avoids the problem of optical cross talk but is optically not as efficient as the coaxial solution. As it is shown in Fig. 1, the overlap function depends on the receiving FOV ϕ, diameter of the telescope's objective lens (or mirror) d_0, divergence

of the emitted laser beam θ, laser-output aperture W_0, and on the distance d_i and tilt angle δ between the two axes [11].

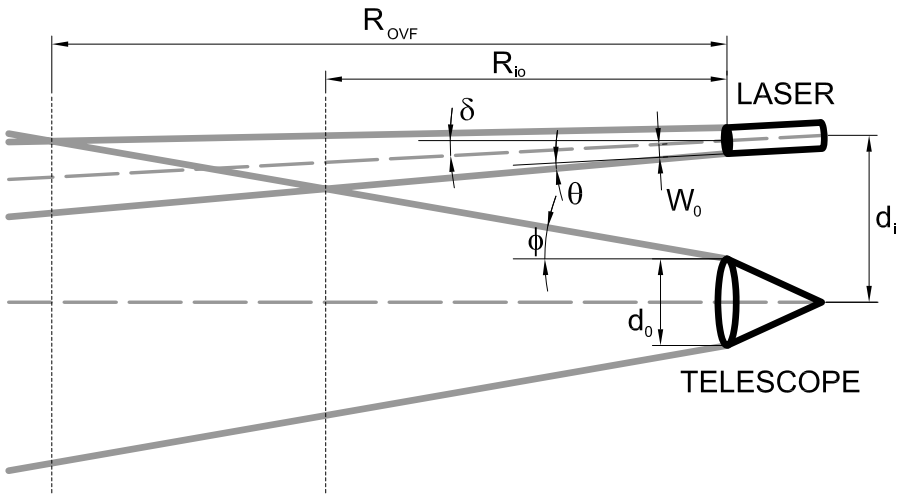

Figure 1. Biaxial configuration scheme for a lidar ceilometer. R_{io} stands for the initial range at which partial overlap between the laser beam and the telescope's FOV begins. R_{OVF} is the starting range of full overlap.

The state-of-the-art technological values discussed so far are summarized in Table I.

III. PERFORMANCE ASSESSMENT

In this section, a link-budget simulation has been developed to tune the ceilometer design parameters within the design intervals of Table I. The simplified Mie/Rayleigh atmospheric model of Fig. 2, corresponding to a wavelength of 905 nm, has been used in the simulations, its main limitation being the use of a constant molecular background. This model assumes "standard-clear" atmospheric conditions (visibility equal to 23.5 km as in [11]) inside the boundary layer (0-3 km height). At this point, note that Fig. 2 represents total opto-atmospheric parameters defined as

$$\alpha^{tot}(R) = \alpha^{aer}(R) + \alpha^{mol}(R), \tag{1}$$

$$\beta^{tot}(R) = \beta^{aer}(R) + \beta^{mol}(R), \tag{2}$$

Table I. Intervals of acceptable values for the main ceilometer design parameters based on a state-of-the-art study.

PERFORMANCE		Maximum detection range, R_{max}	7500 m
		Range resolution, ΔR	< 30 m
EMITTER	Laser	Type	High repetition rate laser
		Wavelength, λ	905 nm
		Pulse Energy, E_0	1-10 μJ
		Pulse duration, τ_L	10-150 ns
RECEIVER	Photodetector	Type (Si-APD)	Silicon Avalanche Photodiode
	module	Intrinsic responsivity, R_{io}	0.30-0.62 $A\,W^{-1}$ (QE : 40-85 %)
		Gain, M	30-250
		Photosensitive diameter, d_D	0.25-5 mm
		Noise Equivalent Power, NEP_m	20-700 $fW\,Hz^{-1/2}$
	Optics	Primary lens diameter, d_0	100-200 mm
		Field of view, ϕ	1-5 $mrad$ (half angle)

where α and β stand respectively for extinction and backscatter, and superscripts tot, aer and mol are reminders for $total$, $aerosol$ and $molecular$ components.

A. Signal-to-Noise Ratio (SNR) Simulations

The expression of the signal-to-noise ratio for a typical APD and TIA combination is given by [23]

$$SNR(R) = \frac{R_{io} M G_T \xi_0 \xi P(R)}{\sqrt{\left[\sigma^2_{sh,s}(R) + \sigma^2_{sh,d} + \sigma^2_{th}\right] \cdot B_N}}, \tag{3}$$

in units of $[V/V]$, where $R_{io}[A\,W^{-1}]$ is the APD current intrinsic responsivity, M is the APD multiplication factor, $G_T[\Omega]$ is the receiver transimpedance gain, ξ_0 is the total transmission factor of the receiving optics at the design wavelength λ_0 ($\xi_0 = \xi(\lambda_0)$), $P(R)[W]$ is the backscattered signal power, $\xi(R)$ is the overlap factor, and $\sigma^2_{sh,s}$, $\sigma^2_{sh,d}$ and σ^2_{th} are the photo-induced shot noise, the dark-shot noise and the thermal noise, respectively $[V^2 Hz^{-1}]$,

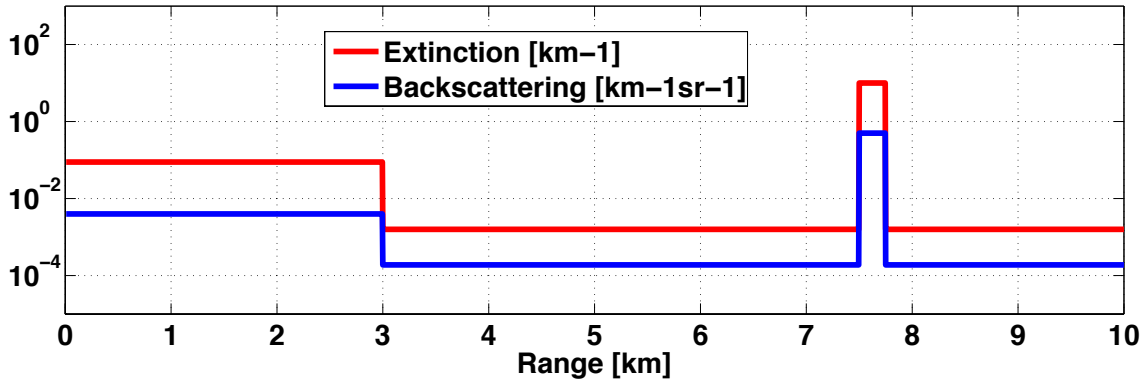

Figure 2. Simplified opto-atmospheric model for the total extinction (*aerosol* + *molecular* components) and total backscatter parameters at a wavelength of 905 nm. The model [11, 24] uses a "standard-clear" homogeneous atmosphere (α^{aer} =0.087 km^{-1}, β^{aer} =3.8×10^{-3} $km^{-1}sr^{-1}$) inside the boundary layer (0-3 km height) and locates a light-water cloud (α^{aer} =10 km^{-1}, β^{aer} =0.5 $km^{-1}sr^{-1}$) layer in the 7.5-7.75 km range. A constant molecular background (α^{mol} =1.6 ×10^{-3}km^{-1}, β^{mol} =1.9×10^{-4} $km^{-1}sr^{-1}$) is also used.

and $B_N[Hz]$ is the equivalent noise bandwidth in reception.

These noise spectral densities are computed as follows [23],

$$\sigma^2_{sh,s}(R) = 2qG_T^2FM^2R_{io}\xi_0\big[P(R)\xi(R) + P_{back}\big], \tag{4}$$

$$\sigma^2_{sh,d} = 2qG_T^2(I_{ds} + FM^2I_{db}), \tag{5}$$

$$\sigma^2_{th} = \sigma_{th,i}G_T^2, \tag{6}$$

all in units of $[V^2\ Hz^{-1}]$, where F is the excess noise factor, $P_{back}[W]$ is the background radiance power, $I_{ds}[A]$ is the APD surface dark current, $I_{db}[A]$ is the APD bulk dark current, $\sigma^2_{th,i}[A\ Hz^{-1/2}]$ is the amplifier input noise current density and $q[C]$ is the electron charge. All other variables have already been presented.

The return power component is computed from the well-known single-scattering form of the elastic lidar equation [24],

$$P(R) = K_sU(R), \tag{7}$$

with

$$U(R) = \frac{\beta(R)}{R^2} \exp^{-2\int_0^R \alpha(r)dr}, \tag{8}$$

where $\beta(R)[m^{-1}sr^{-1}]$ is the total atmospheric volume backscattering coefficient, $R[m]$ is the range, $\alpha(R)[m^{-1}]$ is the total atmospheric volume extinction coefficient. The system constant $K_s[W\ m^3]$ is a key parameter for determining the performance of a lidar system and allowing easy comparison with other instruments, and is given by

$$K_s = \frac{E_0 A_r c}{2}, \tag{9}$$

where $E_0[J]$ is the energy emitted per laser pulse, $A_r[m^2]$ is the effective receiver area and $c[m\ s^{-1}]$ the speed of light.

The background-radiance power component accepted by the receiving optics is computed as [11]

$$P_{back} = L_b K_b, \tag{10}$$

where $L_b[W\ m^{-2}\ nm^{-1}\ sr^{-1}]$ is the sky background spectral radiance and $K_b[m^2\ nm\ sr]$ is defined here as the background-radiance system constant given by

$$K_b = A_r \Omega_r \Delta\lambda, \tag{11}$$

where $\Omega_r[sr]$ is the receiver-system acceptance solid angle ($\Omega_r = \pi \sin^2(\phi) \sim \pi\phi^2$ (i.e. $\phi \ll 0$), [33]) and $\Delta\lambda[nm]$ is the interference filter bandwidth.

The noise equivalent power of the photoreceiver module is computed as [25]

$$NEP_m = \frac{\sqrt{\sigma_{sh,d}^2 + \sigma_{th}^2}}{R_{io} M G_T}, \tag{12}$$

in units of $[W\ Hz^{-1/2}]$, where all other variables have already been presented.

Substituting Eqs. 4, 7, 10 and 12 into Eq. 3 and operating, the following expression is obtained for the SNR,

$$SNR(R) = \frac{\xi_0 K_s U(R)}{\sqrt{\left[\frac{2qF}{R_{io}}(K_s U(R) + K_b L_b)\xi_0 + NEP_m^2\right] \cdot B_N}}, \tag{13}$$

where a full overlap factor, $\xi(R)$ =1 has been assumed.

After averaging N signal pulses, the SNR improves by a factor $\sqrt{N}$ provided that the noise realizations are independent and the atmosphere stationary within the integration time. That is,

$$SNR(R) = \frac{K'_s U(R) S_p}{\sqrt{\frac{2qF}{R_{io}}\left[K'_s U(R) + K'_b L_b\right] + NEP_m^2}}, \tag{14}$$

where $K'_s = \xi_0 K_s$, $K'_b = \xi_0 K_b$, and S_p is a scaling parameter computed as

$$S_p = \sqrt{\frac{N}{B_N}}, \tag{15}$$

where N is the number of integrated pulses and B_N the noise-equivalent bandwidth in reception. In Eq. 14 the SNR is expressed as a function of 5 parameters, where K'_s and K'_b are characteristic constants of the lidar system while NEP_m, R_{io} and F are variables that only depend on the receptor module used. It is worth to note that in order to increase the SNR one can increase the number of integrated pulses but one can also decrease the noise-equivalent bandwidth.

As stated in Section II, the photodetector module in this prototype is a combination of a *Si-APD* and a TIA. The photosensitive surface typically has diameters (d_D), ranging from 0.25 to 5 mm (Table I). The equivalent bandwidth B_N of the photodetector module must be greater than 2.5 MHz in correspondence with the specified range resolution ΔR <30 m (Table I), assuming a pulse duration of τ_l ≥10 ns (Table I) and a sampling frequency of $f_s = 2B_N$ (Nyquist criterion).

The chosen photodetector module is the Hamamatsu C5331-04 model [26], with photosensitive diameter d_D =3 mm, noise equivalent power (NEP_m) of 400 $fW\ Hz^{-1/2}$ and intrinsic responsivity (R_{io}) equal to 0.327 A/W. The excess noise factor (not specified by the manufacturer) is estimated at F =2.77, where the empirical formula $F = M^x$ [27] has been applied, with M =30 being the gain [26] and x =0.3 the excess noise index [28]. The commercial photodetector module has a bandwidth of 80 MHz. As the SNR is inversely proportional to the square root of the bandwidth (Eqs. 14 and 15) one can improve the SNR by applying a low-pass digital filter to the receiver output signal. In the simulations presented next a filter cut-off frequency, $f_c = 3\ MHz$ is used, which yields a noise-equivalent bandwidth, $B_N = 3\ MHz$ in Eq. 15. Similar bandwidths are used by other commercial

ceilometers [5].

From Eq. 15, a scaling parameter S_p=0.224 is obtained with B_N =3 MHz and N =150000 signal pulses averaged. The latter value corresponds to an observation time equal to 30 s (temporal resolution used by the ceilometer network of the German Meteorological Service [30]) and a typical PRF equal to 5 kHz. A spectral radiance of $L_b = 10^{-2}\ W\,m^{-2}\,nm^{-1}\,sr^{-1}$ at 905-nm wavelength, corresponding to the diffuse component of typical background radiance, has been assumed [11].

In the SNR simulations presented below the system constant K'_s and the background-radiance system constant K'_b have been tuned according to the variants shown in Table II. The system constant (K'_s) takes values ranging from 0.5 to 20 Wm^3, where in Eq. 9 pulse energies (E_0) between 1 and 10 μJ (Table I) are assumed as well as receiving diameters d_0 ranging from 100 to 200 mm (Table I). The background-radiance system constant takes two values, K'_b =2.5 $\cdot 10^{-5}$ and $2{\cdot}10^{-7}$ $m^2 nm\,sr$, which respectively correspond to configurations with low and moderate rejection of background radiation. Receiving diameters of d_0 = 200 and 150 mm, fields of view (half-angle) of ϕ =5 and 1 $mrad$, and interference filter widths of $\Delta\lambda = 25$ and 10 nm are assumed respectively for each configuration in Eq. 11. A higher drop in K'_b would not entail significant improvements in the SNR since for $K'_b \leq 2{\cdot}10^{-7}$ $m^2 nm\,sr$ the dark-shot and the thermal-noise terms dominate over the photo-induced noise variance (Eqs. 4-6). A typical receiving optics transmission factor ξ_0 =0.4 is assumed in all the variants.

Table II. Parameters considered in the SNR simulations.

Variant number	System constant $K'_s[Wm^3]$	Background-radiance system constant $K'_b[m^2 nm\,sr]$
1	20	$2{\cdot}10^{-7}$
2	2	$2{\cdot}10^{-7}$
3	0.5	$2{\cdot}10^{-7}$
4	20	$2.5{\cdot}10^{-5}$
5	2	$2.5{\cdot}10^{-5}$
6	0.5	$2.5{\cdot}10^{-5}$

Fig. 3(a) shows the simulations of the SNR for variants 1 to 6 of Table II. Also represented is the value SNR_{goal} =5. This threshold has been considered sufficient to apply an automatic cloud detection algorithm. For example, the $STRAT$ algorithm [31] uses a SNR threshold equal to 3 to determine where the signal is strong enough to extract information. It can be seen that for all variants the SNR progressively decreases over the 0-3 km range, corresponding to the planetary boundary layer (PBL). At the end of the PBL, a sharp fall in SNR can be observed as result of the disappearance of Mie backscattering, with only the component of molecular origin remaining. Likewise, the SNR peaks can be observed at an altitude of 7.5 km, corresponding to the light water cloud simulated at this range. These peaks can be seen in greater detail in Fig. 3(b).

A clear correlation can be observed in Fig. 3(b) between the SNR peak due to the cloud and the system constant K'_s. Therefore, when the system constant takes low values, K'_s =0.5 Wm^3 (variants 3 and 6), the threshold SNR_{goal} =5 is not reached, while for high values, K'_s =20 Wm^3 (variants 1 and 4), the cloud is detected. For K'_s =2 Wm^3 (variants 2 and 5) it can be seen how the SNR value approaches 5 as background-radiation rejection improves (K'_b decreases). For variant 2 a SNR equal to 5.66 is achieved (equivalent to a SNR of 3 considering an observation time of 10 s).

From the above results, it can be concluded that the system constant K'_s must be of the order of 2 Wm^3, since for lower values, K'_s =0.5 Wm^3, the required detection sensitivity is not reached, and for higher values, K'_s =20 Wm^3, the system would become unnecessarily oversized and expensive. For eye-safety reasons in the developed prototype, the energy emitted per laser pulse was limited to E_0 =1.76 μJ (see Sect. IV), and a receiving diameter of d_0 =150 mm was used to ensure the specified system constant K'_s =2 Wm^3.

B. Overlap Factor (OVF) Simulations

The overlap factor (OVF) is defined as the fraction of the illuminated atmospheric cross section at a distance R that is viewed by the receiving optics [11],

$$\xi(R) = \frac{A\{r_T(R, W(R); d(R))\}}{\pi W^2(R)}, \tag{16}$$

where $A[m^2]$ is the area overlap function, $r_T(R)[m]$ is the radius of the receiver-optics FOV in the target plane, $W(R)[m]$ is the radius of the laser pulse in the target plane and $d(R)[m]$

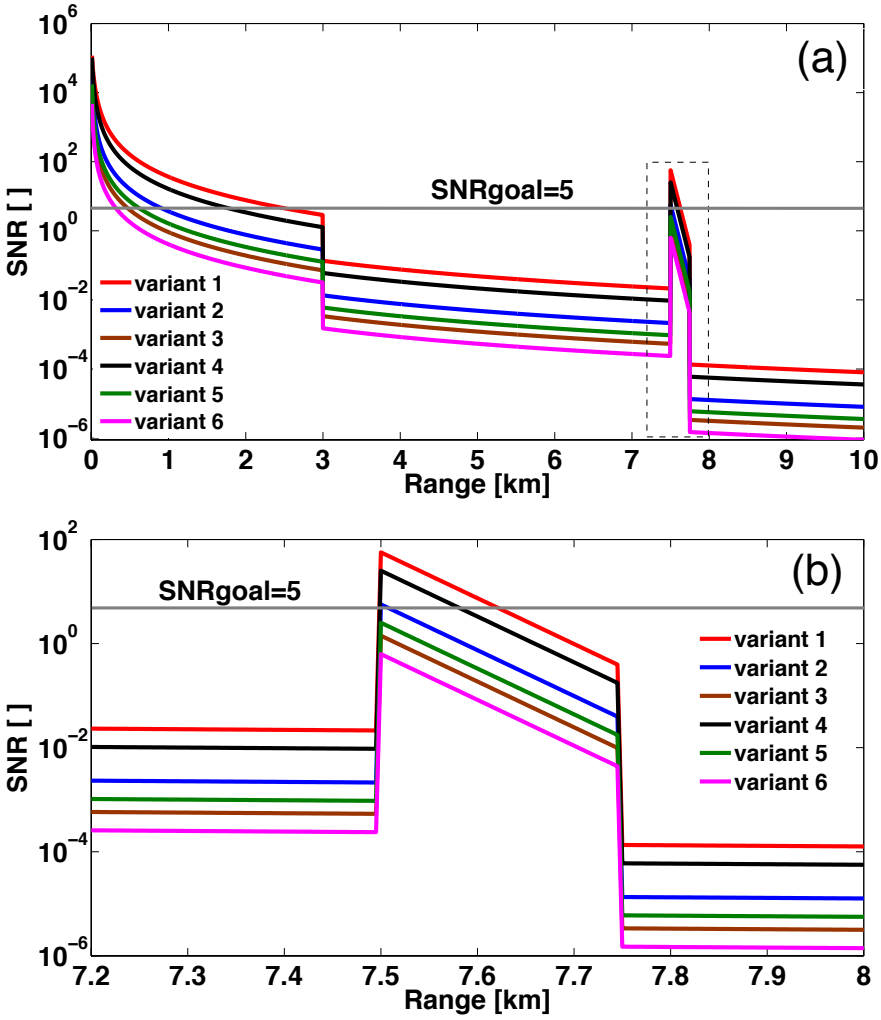

Figure 3. Signal-to-noise ratio simulations under Mie/Rayleigh atmospheric model. (a) Signal-averaged range-dependent SNR. (b) Signal-averaged range-dependent SNR due to a light-water cloud layer in the 7.5-7.75 km range for variants 1 to 6 (Table II).

is the separation of the emission and reception axes in the target plane. It is worth to note that we have calculated the overlap factor by taking into account only geometrical factors on the illuminated atmospheric target plane. In this reasoning we assume that the entrance pupil of the telescope is the telescope aperture (i.e., the imaging properties of the receiving optics do not affect the OVF or, in other words, the OVF can indistinctly be computed at the atmosphere plane or at the detector plane. See also Sect.IV B, Fig. 7).

By following [11], the overlap factor can be expressed as a function of geometrical and optical parameters of the lidar system,

$$\xi(R) = f(\phi, \theta, \delta, d_0, W_0, d_i), \tag{17}$$

where all the parameters have been presented in Sect. II and Fig. 1.

The geometry of a biaxial lidar is shown in Fig. 4 when the emission and reception axes are divergent (δ <0) and convergent (δ >0). It can easily be deduced that to achieve full overlap the following expression must be satisfied

$$-(\phi - \theta) \leq \delta \leq (\phi - \theta), \tag{18}$$

from which it is clear that the half-angle FOV, ϕ must be greater than the laser beam divergence, θ and that they can only take equal values when the two axes are parallel.

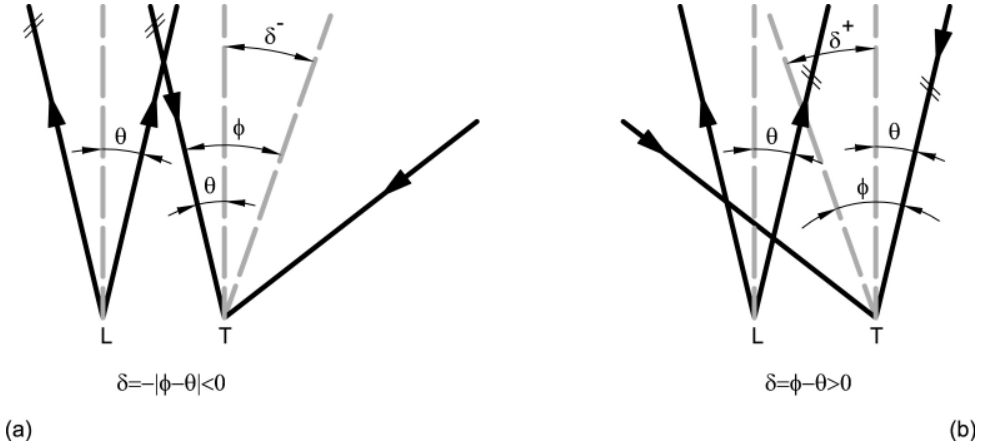

Figure 4. Geometry of a biaxial lidar where "L" stands for laser and "T" stands for telescope. (a) Laser and telescope axes are divergent. (b) Laser and telescope axes are convergent.

In the following simulations a study is carried out on the variation of the overlap factor, Eq.17, with the receiving FOV ϕ, the laser-beam divergence θ and the tilt angle δ according to the values given in Table III. Values ranging from ϕ =1 to 5 $mrad$ (Table I) are considered for the FOV. Similarly, laser beam divergences (θ) between 0.75 and 4.75 $mrad$ are assumed, though in all the variants the condition $\phi > \theta$ is met. For the tilt angle δ, the cases of parallel (δ =0 $mrad$) and convergent (δ =1 $mrad$) optical axes are considered. The case of divergent

optical axes is not considered, as it is clear from Fig. 4 that the range of full overlap R_{OVF} is lower when the axes converge than when they diverge.

For all variants an effective radius of the receiving optics of r_0 =75 mm (Section III A) is assumed, as well as a distance between axes of d_i =150 mm and a transmitter output laser beam radius of W_0 =150 μm, which is a standard value in laser diodes. The value of the distance between axes d_i is set bearing in mind that, on one hand, minimizing this distance is of interest because the range of full overlap R_{OVF} lowers when d_i decreases [11]. On the other hand, d_i must be greater than the sum of the radii of the receiving optics, r_0 =75 mm (Section III A) and emission optics, r_e =25 mm (Section IV). To regulate this distance a translational platform is used in the designed ceilometer prototype.

Table III. Parameters considered in the overlap factor simulations for tilt angles δ =0 and 1 $mrad$.

Variant number	Field of view ϕ $[mrad]$	Laser divergence θ $[mrad]$
$1'$	5	4.75
$2'$	5	2.75
$3'$	5	0.75
$4'$	3	2.75
$5'$	3	0.75
$6'$	1	0.75

Figure 5 represents the OVF simulations, which correspond to totally parallel emission and reception optical axes (i.e. δ =0 $mrad$). In this case, full overlap is achieved provided the FOV is greater than the laser-beam divergence, $\phi > \theta$, as established for all the variants considered. When the value of the divergence approaches to the FOV (variants $1'$, $4'$ and $6'$), full overlap is achieved at further ranges, between 200 and 300 m. The lowest range of full overlap, R_{OVF} =20 m is achieved for the combination of a wide FOV, ϕ =5 $mrad$, with a narrow laser beam divergence, θ =0.75 $mrad$ (variant $3'$).

Figure 6 shows the OVF simulations when the optical axes have a misalignment, δ =1 $mrad$ (i.e., convergent axes). For variants $1'$, $4'$ and $6'$ the difference between the

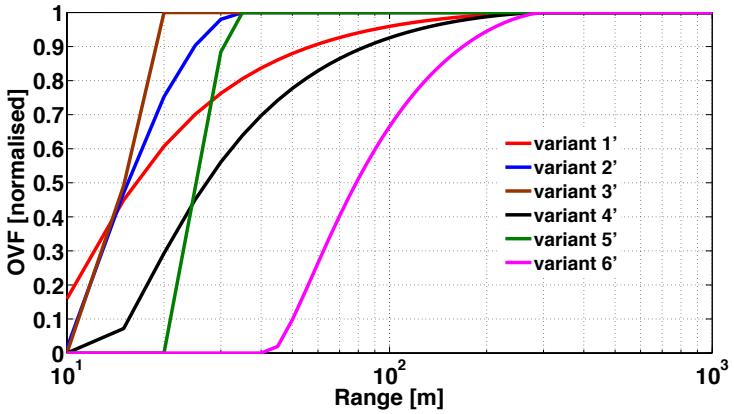

Figure 5. Normalized overlap factor (OVF) versus range for variants $1'$ to $6'$ (Table III). Tilt angle δ =0 $mrad$ (parallel axes).

FOV and laser beam divergence is $\delta > \phi - \theta$ and Eq. 18 is not satisfied. In these cases, full overlap is only achieved for an interval of ranges between approximately 60 and 200 m, while at further ranges the overlap is partial. For the remaining variants ($\delta < \phi - \theta$) full overlap occurs at closer ranges than when the optical axes are totally parallel (δ =0 $mrad$), with the most favorable case being variant $3'$ (ϕ =5 $mrad$, θ =0.75 $mrad$), in which R_{OVF} =15 m.

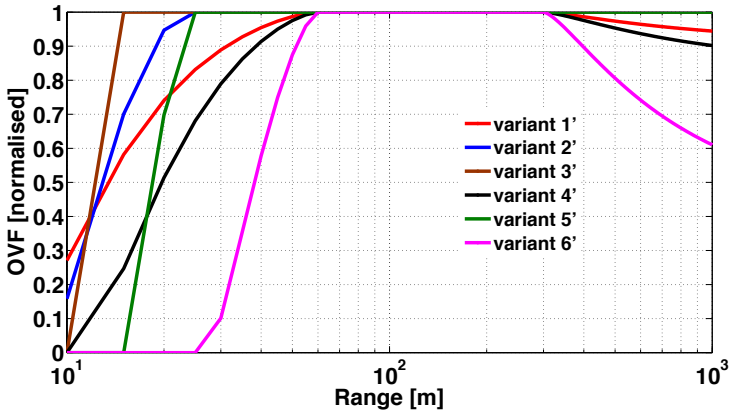

Figure 6. Normalized overlap factor (OVF) versus range for variants $1'$ to $6'$ (Table III). Tilt angle δ =1 $mrad$ (convergent axes).

To select the most adequate FOV ϕ, it needs to be borne in mind that low FOV values allow reduction of the background radiation whereas high values in combination with narrow laser divergences, allow low ranges of full overlap. In addition, for high FOV figures it is possible to use large-area APD's, an option that is preferred in order to avoid high-precision focusing onto the receiving detector. For the above reasons, a relatively high FOV (around 5 $mrad$) is chosen to permit low-range operation, while background radiation rejection is achieved by using a narrow-band interference filter. The laser divergence has to be minimized (θ <2.75 $mrad$) to reduce the height of full overlap, but considering the trade-off that this parameter was on the eye-safety considerations discussed in Section IV. As in the previous simulations, it is obtained that the lowest range of full overlap corresponds to a tilt angle of δ =1 $mrad$. In the prototype a gimbal device has been implemented to adjust this angle (Table IV).

IV. OPTO-MECHANICAL OVERVIEW

The opto-mechanical configuration of the lidar ceilometer prototype developed by the authors is presented below. The final specifications of this configuration correspond to the results of the parametric simulations discussed in Section III.

A. Emission subsystem

The emission source used is a 3B-class $InGaAs$ 905 nm wavelength, 1.76 μJ-pulse energy, 5 kHz rep. rate laser diode characterized by a high divergence. In order not to overspill emission power, a convergent lens has been used at the laser output to reduce the emission divergence down to 2.27 $mrad$, a lower figure than the receiver FOV (ϕ =4.92 $mrad$, Table IV). To ensure an eye-safe system this convergent lens has been selected in accordance with IEC-60825 standard [14]. Considering the conservative hypothesis of a point laser source, the output laser beam must meet the following three requirements in order not to exceed the Maximum Permissible Exposure (MPE) value:

- Human eye exposure to any laser pulse must be no higher than the MPE level for a single pulse,

$$H_{single} = 5 \cdot 10^{-3} \times C_4 = 12.9 \, \frac{mJ}{m^2}, \tag{19}$$

where the correction factor C_4 =2.57 for λ =905 nm is given in Ref. [14].

- Mean exposure to laser pulse train of duration T must be no higher than the MPE level for a single pulse of duration T,

$$H_T = 18 \times T^{-0.25} \times C_4 = 260 \, \frac{J}{m^2}, \tag{20}$$

where a typical value T =10 s has been used [14]. So, the exposure for a single pulse is

$$H_{single,mean} = \frac{H_T}{N} = 5.2 \, \frac{mJ}{m^2}, \tag{21}$$

where N =5·10^4 is the number of pulses for a duration T assuming PRF=5·10^3 Hz (Table IV).

- Exposure to any single pulse of the pulse train must be no higher than the MPE level for a single pulse multiplied by a correction factor $N^{-0.25}$. Factor $N^{-0.25}$ is aimed at correcting the threshold for high repetition rates. That is,

$$H_{train} = H_{single} \times N^{-0.25} = 0.859 \, \frac{mJ}{m^2}. \tag{22}$$

From Eqs. 19-22 above, it is obvious that Eq. 22 gives the most restrictive MPE (energy density threshold). Combining this MPE threshold with the 1.76 μJ laser output energy (Table IV), it is found that the output laser-beam aperture radius must be greater than 25.5 mm. The ceilometer uses a standard-size convergent lens of 50 mm diameter placed at f_e =75 mm from the diode laser window as the effective emission aperture. Therefore, the laser spot size on the effective emission aperture is

$$r_{se} = f_e \tan(\theta_\perp) = 27.3 \, mm, \tag{23}$$

where r_{se} is the laser spot radius on the convergent lens (effective emission aperture), f_e =75 mm (Table IV) is the convergent lens focal distance and $\theta_\perp$ =20^o is the laser beam maximum divergence. The resultant system is therefore eye-safe although, since a standard size of lens has been chosen, slight energy losses occur in transmission as the laser beam section is slightly larger than the selected lens. It should be mentioned that since the transverse distribution of the laser light is Gaussian, losses will be lower than the nominal ones predicted assuming uniform illumination ($\sim$ 16%).

B. Receiving subsystem

Figure 7 is a sketch of the designed receiving optical system, which is used to focus the backscattered light onto the photodetector surface, a Hamamatsu C5331-04 silicon APD module (Table IV). A Fresnel lens (L_1) is used as the system objective as it is a low-cost solution characterized by a low f number and reduced absorption. Another recent application of Fresnel lenses in lidar systems can be found in [32]. L_1 is followed in the receiving system by the divergent collimating lens (L_2) so as to ensure that the incoming light rays are incident in the normal direction on the 10 nm interference filter ($FILT$) surface, otherwise detuning of the spectral response of the filter occurs. Next, convergent lens (L_3) is used to focus filtered light onto the APD.

Though practical implementation of the receiving system enables adjustment of distances d_1 and d_2 in Fig. 7, their nominal setting is the confocal arrangement $d_1 = |f_1| - |f_2|$, $d_2 = |f_2| + |f_3|$ and $d_3 = |f_3|$. Using matrix ray-propagation analysis [33], it is possible to derive the equivalent focal length of the receiving optical system as

$$f_{eq} = \frac{f_1 f_3}{f_2}, \tag{24}$$

where f_{eq} is the equivalent focal length, f_1 is the primary convergent lens focal length (L_1: Fresnel), f_2 is the divergent lens with focal length (L_2) and f_3 is the convergent lens focal length (L_3).

If, as is the case, we impose the design condition $f_2 = f_3$, the receiving FOV ϕ becomes

$$\phi = \frac{r_D}{f_{eq}} = \frac{r_D}{f_1} = 4.92\, mrad, \tag{25}$$

where r_D =1.5 mm is the APD radius.

As an introduction to the designed prototype, Fig. 8(a) shows the mechanical structure containing the optical systems presented above. The cross-section of the receiving opto-mechanical system is depicted in Fig. 8(b). The blocks (2), (3) and (4) correspond to the block L_2-$FILT$-L_3 in Fig. 7. The opto-mechanical structure features regulation capacity by means of the knob (11). Adjustment of the APD-to-focal-plane distance d_3 (i.e., L_3-to-APD distance) and its operation is as follows: by turning the focal distance regulator knob (11), the focal distance regulator axis (10) screws into the APD support frame (7) and causes vertical movement of the APD receiver module (9). As a result the photodetector surface

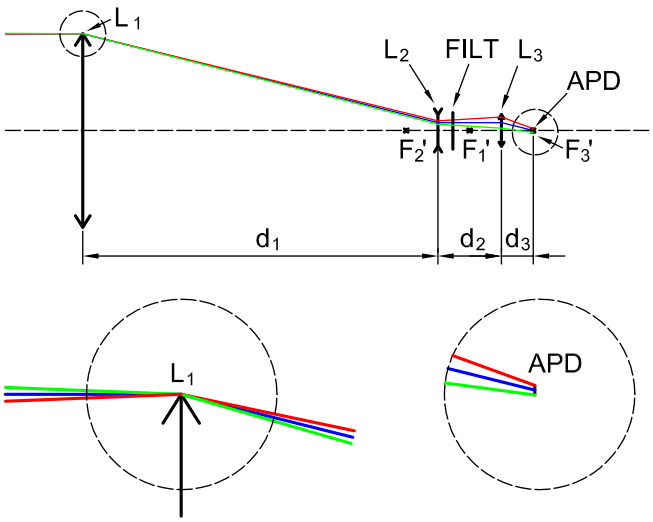

Figure 7. (Color online) Ceilometer optical receiving chain scheme (see also Table IV). (L_1) Primary lens (Fresnel), (L_2) divergent lens, ($FILT$) interference filter, (L_3) convergent lens, (APD) photodetector active area. Distances d_1 (user adjustable), d_2 and d_3 (user adjustable) show the confocal arrangement of the set up, that is L_1, primary-lens image focal point, F_1', and L_2 object focal point, F_2, coincide ($F_1' \equiv F_2$). Likewise, the photodetector is represented as placed in L_3 image focal plane ($d_3 = |f_3|$). Joint block L_2-$FILT$-L_3-APD (see also Fig. 8) can be displaced together in relation to L1 by adjusting d_1. Red and green rays correspond to the maximum FOV accepted by the telescope.

(5) varies its distance to convergent lens L_3 (4). This regulator allows precise positioning of the photodetector surface at L_3 focal plane, thus offsetting any focal-length tolerance.

V. PRELIMINARY PROTOTYPE

A first preliminary low-cost prototype has been developed within the framework of a UPC-DENA S.L. business consortium for remote sensing of cloud-base heights as a cooperative sensor for forecasting storm initiation. This initial experimental prototype is aimed at studying and identifying the critical parameters of the system with a view to a more refined

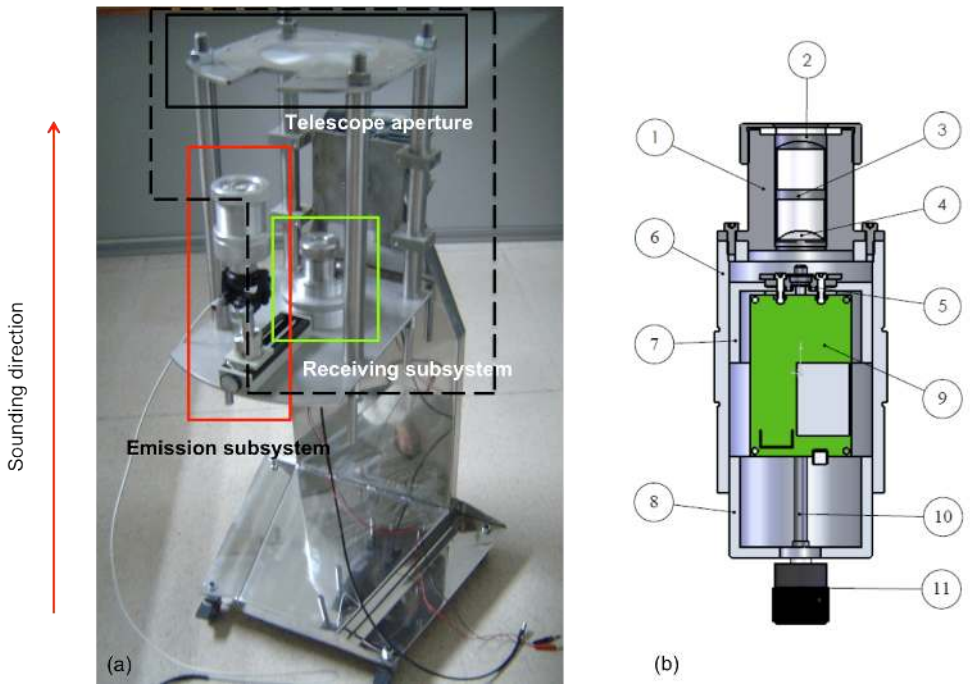

Figure 8. (Color online) Emission/Receiving opto-mechanical configuration. (a) Picture of the ceilometer prototype showing the emission (red box) and receiving (black dashed box) subsystems. (b) Cross-view showing the APD-to-focal-plane regulator mechanism (marked with a green box in (a)). Main components are: (1) receiving lens housing assembly (L_2-$FILT$-L_3), (2) divergent lens L_2, (3) Interference filter ($FILT$), (4) convergent lens L_3, (5) photodetector surface, (6) opto-electronic receiver support, (7) APD receiver module support frame, (8) receiver opto-mechanical lower cover, (9) Si-APD receiver module, (10) convergent-lens focal-distance regulation axis, (11) focal distance regulation knob. See extensive details in [34].

prototype. The constructed lidar ceilometer (Fig. 8) has a high number of degrees of freedom (i.e., many adjustable parts), including amongst others: adjustment of emission and reception optical elements, adjustment of the distance and tilt angle between optical emission and reception axes by means a translational platform and gimbal device, and instrument aim control by means of reducing gear.

The experimental results obtained by our lidar ceilometer are exposed below. Section V A briefly reports the procedure used to detect a topographic target and Sect. V B shows preliminary test measurements for cloud detection, advertising that the system is able to detect

atmospheric echoes at heights up to 7 km with acceptable likelihood as claimed in the link budget simulations.

A. Measurement of a topographic target

To ensure that the lidar ceilometer measures appropriately it was aimed nearly horizontally and pointing to a mountain located at $\sim 1.2km$ (Fig. 9(a)). This measurement was used to adjust the receiving optics and to align the optical axes. Figure 9(b) plots the backscattered power $P(R)$ vs distance and shows a very clear peak located at the distance of the topographic target.

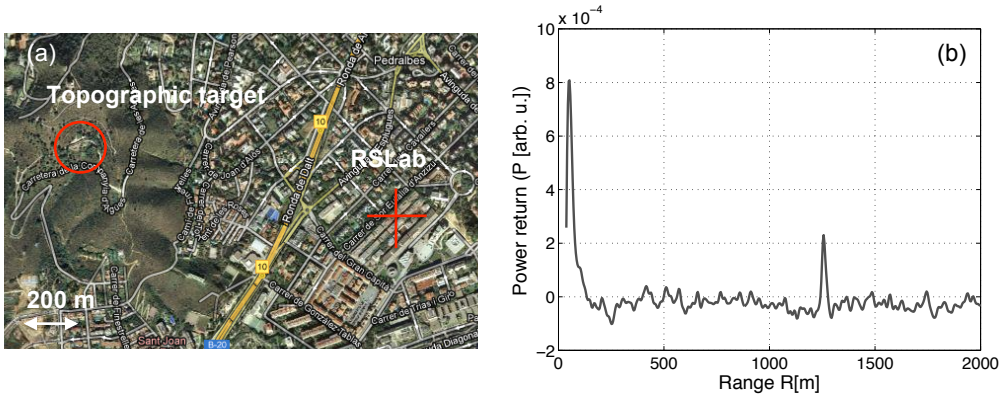

Figure 9. (Color online) Detection of a topographic target with the lidar ceilometer placed at the UPC premises in North Campus (Barcelona). (a) Satellite view of the ceilometer location, as well as location of the mountain. (b) Backscattered power $P(R)$ vs distance. The spatial resolution is 3.75 m and observation time 10 s. The peak located at $\sim$200 m is a detection artifact caused by the rising edge of the OVF (overlap factor smaller than 1), and therefore, not all backscattered light is collected by the photodetector.

B. Cloud detection

Figure 10 presents initial atmospheric measurements obtained with the constructed prototype. In order to enhance the SNR, raw data provided by the photodetector module has been filtered with a 3 MHz cut-off frequency according to the noise-equivalent bandwidth

discussed in Sect. III A. A 3 MHz low-pass FIR filter (FIR stands for Finite Impulse Response) based on the Parks-McClellan algorithm [29] has been used as spatial smoothing. These kinds of linear phase filters are optimal to minimize the maximum error between the desired frequency response and the actual frequency response.

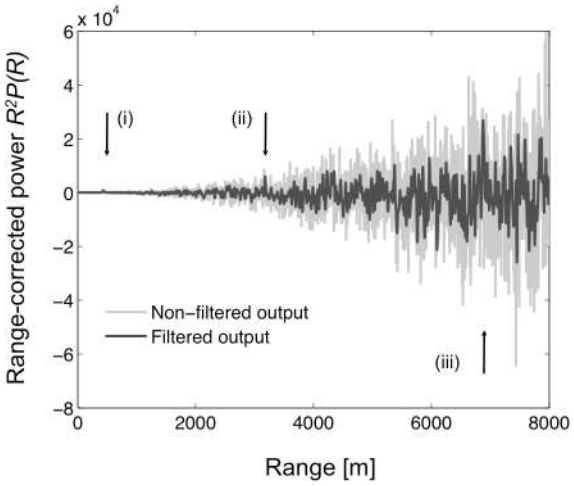

Figure 10. Preliminary test measurement showing detection of a storm low cloud (i) and two possible high clouds (ii) and (iii). Unfiltered (gray solid line) and filtered (black solid line) range-corrected power return, $R^2 \cdot P(R)$ vs distance. The spatial resolution is 3.75 m and the observation time 10 s.

Figure 10 compares the range-corrected received power before (gray solid line) and after applying the smoothing filter (black solid line). In both representations we can clearly distinguish a light-rain cloud (i.e., optically thin) located at $\sim$400 m, which is in accordance with the data provided by the Catalan Meteorological Service (SMC) ($\sim$1 mm/h). However, only in the filtered output two small peaks (not observed in the non-filtered data) located at 3200 m and 6900 m are evidenced. It is worth to note that after applying the filter the SNR has increased but at the expense of a lower spatial resolution.

Figure 11 shows in better detail the range-corrected peaks detected with the ceilometer. The estimated SNR at the cloud peak located at $\sim$ 400 m is SNR =25.6, value that has been estimated by computing the ratio between the intensity at the cloud peak (420 m) and the noise-standard deviation in its vicinity. The noise standard deviation has been computed

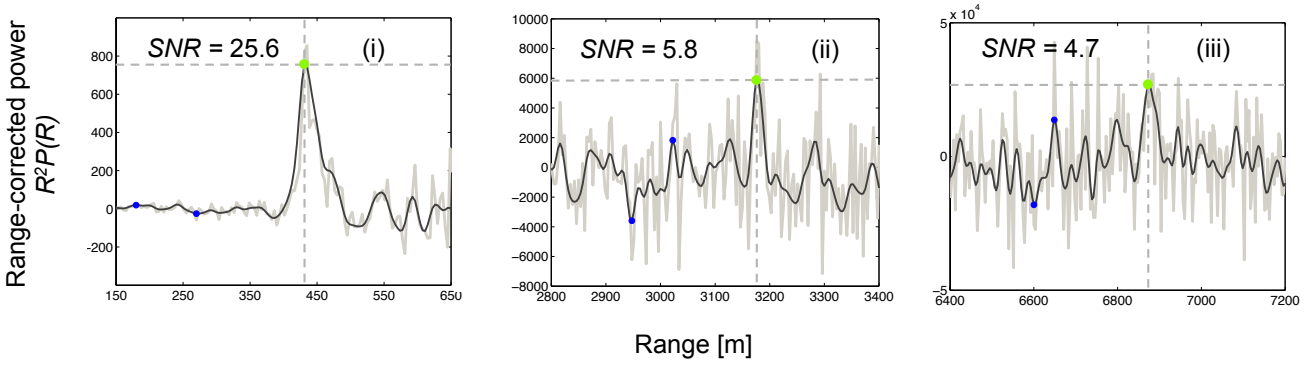

Figure 11. (Color online) Range-corrected power, $R^2 \cdot P(R)$ vs distance. Panels (i), (ii) and (iii) show the detected peaks in better detail. Green dots mark the absolute maximum of the peak, and the blue dots the relative maximum and minimum of the background noise in the vicinity of the peak.

by assuming Gaussian statistics and by averaging the 6-σ noise amplitude (equivalently, $\pm$3-σ noise amplitude) at the approximate cloud base (350 m). Details on the piece-wise SNR estimator can be found in Ref. [35]. The estimated SNR for the peak located at 3200 m is 5.8 and has a qualitatively small false-alarm probability [36] while for the peak at 6900 m the estimated SNR is 4.7 and the associated false alarm probability can comparatively be considered moderate/moderate-to-high.

The system specifications of our ceilometer prototype are summarized in Table IV.

Table IV. Main characteristics of the designed prototype.

EMITTER	Laser	Model	Laser components (IRLM-080-0104S12)
		Wavelength, λ	905 nm
		Pulse Energy, E_0	1.76 μJ
		Pulse duration, τ_L	10.1 ns
		Pulse repitition frequency, PRF	$\leq$ 5 kHz
	Optics	Lens diameter, d_0	50 mm
		Focal length, f_1	75 mm
		Output beam divergence, θ	2.27 $mrad$ (half angle)
RECEIVER	Optics	Primary lens diameter, d_0	152.4 mm
		Equivalent focal length, f_{eq}	304.8 mm
		Focal number, $f_n = \frac{f_{eq}}{d_0}$	2
		Field of view, ϕ	4.92 $mrad$ (half angle)
	Interference	Center wavelength, λ	905 nm
	Filter	interference filter bandwidth, $\Delta\lambda$	10 nm
	APD	Model	Hamamatsu C5331-04
		Active area, d_D	3 mm
		Spectral response range	400 to 1000 nm
		Responsivity, R_i	9.81 $[A/W]$ (905 nm)
		Noise equivalent power, NEP_m	400 $fW\ Hz^{-1/2}$
		Internal gain, M	30
TILTING	Gimbal	Model	Edmund Optics 25.0 MM ID
REGULATOR		Azimuthal travel / knob rotation	8.33 $mrad$
		Elevation travel / knob rotation	6.41 $mrad$

VI. CONCLUSIONS

Design methodology of an eye-safe 905 nm wavelength, 1.76 μJ-energy, 5 kHz rep. rate, APD-based ceilometer prototype for cloud-base detection has been achieved using parametric simulation. The method uses a convenient analytical reformulation of the range-dependent SNR in a backscatter lidar, Eqs. 14 and 15, and simulation of the laser/telescope overlap function in terms of Eqs. 17 and 18. The modified SNR formulation of Eq. 14 expresses the SNR in terms of the equivalent lidar system constant (K'_s) and background-radiance constant (K'_b), a choice of the opto-electronic receiver (parameter subset given by the receiver(NEP_m), intrinsic responsivity (R_{io}) and excess-noise-factor (F), and specs on the required observation time and spatial resolution (equivalently, the noise equivalent bandwidth) via Eq. 15. Ceilometer characteristic parameters (including a review of opto-electronic receiver parameters) from the technological state of the art at 905 nm are summarized in Table I. Future refinements of the prototype will simplify the mechanical solution presented, hence reducing the degrees of freedom of the adjustable parts presented here (deliberately large for testing purposes).

ACKNOWLEDGMENTS

We thank two anonymous reviewers for their insightful comments on the initial version of this manuscript. The lidar ceilometer prototype has been developed with the financial support of DENA Desarrollos, S.L. The activities on semiconductor lidar technology have been sponsored by MICINN (Spanish Ministry of Science and Innovation) and FEDER (European Regional Development Funds) funds under the $R\&D$ projects, TEC2009-09106, TEC2006-07850/TCM, and AGL2010-22304-C04-03. The Catalan Meteorological Service (SMC) provided the meteorological data in support of the case example presented. Dr. Joan Montanyà (UPC) is also thanked for his cooperation to prepare this work.

---

[1] F. Rocadenbosch, "Lidar-aerosol sensing", in *Enciclopedia of Optical Engineering*, R. G. Driggers, Ed., pp. 1090-1102, Marcel Dekker Inc., New York (2003).

[2] F. T. Ludbrook and J. V. Winstanley, "New laser ceilometer", *IEE J. Electron. Circuits Syst.*, **1**(2), 64-72 (1977).

[3] All weather Inc., "Cloud Height Indicator Laser Ceilometer, Model 8339", User's Manual, California (2005).

[4] Eliason Engineering Inc., "Cloud Ceilometer, Model CBME80", datasheet_available_online, Sweden (Accessed February 2012).

[5] Vaisala Inc., "Ceilometer, Model CL31", User's Guide, Finland (2004).

[6] All Weather Inc., "Cloud Height Indicator Laser Ceilometer, Model 8340", User's Manual, California (2007).

[7] Jenoptik optical systems Inc., "Ceilometer, Model CHM15K-x", datasheet_available_online, Massachusetts, (Accessed February 2012).

[8] Vaisala Inc., "Cloud Height-range Cloud Height detection, Model CL51", datasheet_available_online, Findland, (Accessed February 2012).

[9] Vaisala Inc., "Ceilometer, Model CT25k", User's Guide, Finland (1999).

[10] J. Streicher, C. Werner and W. Dittel, "Design of a small laser ceilometer and visibility measuring device for helicopter landing sites", *Proc. SPIE* **5240**, 31-41 (2004).

[11] R. M. Measures, *Laser Remote Sensing: Fundamentals and Applications*, Krieger Publishing Co, Florida (1992).

[12] MTECH Systems Inc., "Ceilometer Sensor, Model 8200-CHS", datasheet_available_online, (accessed February 2012).

[13] A. M. Kärkkäinen, A.K. Piironen, T. Kähkönen and J. Lönnqvist, "The characteristics and performance of Vaisala's new CT75K lidar ceilometer", *Proc. SPIE* **3104**, 12-17 (1997).

[14] International Electrotechnical Comission, "Safety of laser products - Part 1: Equipment classification and requirements (IEC 60825-1:2007)", Geneva (2007).

[15] J. L. Gaumet, J. C. Heinrich and M. Cluzeau, "Cloud-base height measurements with a single-pulse erbium-glass laser ceilometer", *J. Atmos. Oceanic Technol.*, **15**(1), 37-45 (1998).

[16] Degreane Horizon, "Laser Ceilometer, Model ALC30", datasheet_available_online, France (accessed February 2012).

[17] V. A. Kovalev and W. E. Eichinger, *Elastic Lidar: Theory, Practice, and Analysis Methods*, Wiley-Interscience, New York (2004).

[18] C. Münkel, U. Leiterer and H. Dier, "Affordable lidar for atmospheric aerosol and cloud studies", *Proc. SPIE* **4484**, 198-206 (2002).

[19] Excelitas Technologies Inc, "Long Wavelength Enhanced Silicon APD, Models C30954EH, C30955EH and C30956EH", datasheets_available_online, Massachusetts, (accessed February 2012).

[20] Hamamatsu, "APD Modules", datasheets_available_online, (accessed February 2012).

[21] A. I. Abramochkin and A. A. Tikhomirov, "Optimization of a lidar receiving system. 2. Spatial filters", *Atmos. Oceanic Opt.* **12**, 331-342 (1999).

[22] V. Freudenthaler, "Optimized background suppression in near field lidar telescopes", *Proceedings of the 6th International Symposium on Tropospheric Profiling: Needs and Technologies (ISTP 2003)*, U. Wandinger, R. Engelmann, and K. Schmieder, eds. (Institute for Tropospheric Research), pp. 243-245 (2003).

[23] F. Rocadenbosch, A. Comerón and D. Pineda, "Assessment of lidar inversion errors for homogeneous atmospheres" *Appl. Opt.*, **37**(12), 2199-2206 (1998).

[24] R. T. H. Collis and P. B. Russell, "Lidar Measurement of Particles and Gases by Elastic Backscattering and Differential Absorption", Chap. 4 in *Laser Monitoring of the Atmosphere*, E. D. Hinkley, Ed., pp. 71-151, Springer, Berlin/Heidelberg (1976).

[25] F. Rocadenbosch, "Lidar sensing of the atmosphere: receiver design and inversion algorithms for an elastic system", PhD thesis, Universitat Politècnica de Catalunya, Spain (1996).

[26] Hamamatsu Photonics, "*APD* module, C5331 series", Japan (2007).

[27] Hamamatsu Photonics, "Characteristics and use of *Si-APD*", Japan (2004).

[28] Hamamatsu Photonics, "*Si-APD*, S6045 series", Japan (2005).

[29] McClellan, J.H. Parks, T.W., "A personal history of the Parks-McClellan algorithm", *IEEE, Signal Processing Magazine* **22**(2), 82-86 (2005).

[30] B. Heese, H. Flentje, D. Althause, A. Ansmann and S. Frey, "Ceilometer lidar comparison: backscatter coefficient retrieval and SNR determination", *Atmos. Meas. Tech.* **3**, 1763-1770 (2010).

[31] Y. Morille, M. Haeffelin, P. Drobinski and J. Pelon, "STRAT: An automated algorithm to retrieve the vertical structure of the atmosphere from single-channel lidar data", *J. Atmos. Oceanic Technol.* **24**(5), 761-775 (2007).

[32] R. J. De Young and N. P. Barnes, "Profiling atmospheric water vapour using a fiber laser lidar system", *Appl. Opt.* **49**(4), 562-567 (2010).

[33] K. D. Möller, *Optics*, University Science Books, California (1988).

[34] E. Gregorio, F. Rocadenbosch and A. Comerón, "905-nm biaxial lidar ceilometer prototype", *Proc. SPIE* **6362**, 63621L1-12 (2006).

[35] M. N. M. Reba, F. Rocadenbosch, M. Sicard, C. Muñoz, and S. Tomás, "Piece-wise variance method for SNR estimation in elastic/Raman lidar signals", *Proc. IGARSS*, 3158-3161 (2007).

[36] M. I. Skolnik, "Detection of Signals in Noise", Chap. 5 in *Introduction to Radar Systems*, McGraw-Hill, pp. 276-312 New York (2001).

LIST OF FIGURES